Preexisting Immunity Drives the Response to Neoadjuvant Chemotherapy in Esophageal Adenocarcinoma

Giuseppina Arbore[1,2], Luca Albarello[3], Gabriele Bucci[4], Marco Punta[4,5], Andrea Cossu[6], Lorella Fanti[7], Aurora Maurizio[4], Francesco Di Mauro[1], Vito Bilello[1], Gianluigi Arrigoni[3], Silvia Bonfiglio[4], Donatella Biancolini[4], Francesco Puccetti[2,6], Ugo Elmore[2,6], Luca Vago[5,2], Stefano Cascinu[2,8], Giovanni Tonon[2,4], Riccardo Rosati[2,6], Giulia Casorati[1], and Paolo Dellabona[1]

ABSTRACT

Current treatment for patients with locally advanced esophageal adenocarcinoma (EAC) is neoadjuvant chemotherapy (nCT), alone or combined with radiotherapy, before surgery. However, fewer than 30% of treated patients show a pathologic complete response to nCT, which correlates with increased 5-year survival compared with nonresponders. Understanding the mechanisms of response to nCT is pivotal to better stratify patients and inform more efficacious therapies. Here, we investigated the immune mechanisms involved in nCT response by multidimensional profiling of pretreatment tumor biopsies and blood from 68 patients with EAC (34 prospectively and 34 retrospectively collected), comparing complete responders versus nonresponders to nCT. At the tumor level, complete response to nCT was associated with molecular signatures of immune response and proliferation, increased putative antitumor tissue-resident memory CD39$^+$ CD103$^+$ CD8$^+$ T cells, and reduced immunosuppressive T regulatory cells (Treg) and M2-like macrophages. Systemically, complete responders showed higher frequencies of immunostimulatory CD14$^+$ CD11c$^+$ HLA-DR^{high} cells, and reduced programmed cell death ligand 1–positive (PD-L1$^+$) monocytic myeloid-derived suppressor cells, along with high plasma GM-CSF (proinflammatory) and low IL4, CXCL10, C3a, and C5a (suppressive). Plasma proinflammatory and suppressive cytokines correlated directly and inversely, respectively, with the frequency of tumor-infiltrating CD39$^+$ CD103$^+$ CD8$^+$ T cells. These results suggest that preexisting immunity in baseline tumor drives the clinical activity of nCT in locally advanced EAC. Furthermore, it may be possible to stratify patients based on predictive immune signatures, enabling tailored neoadjuvant and/or adjuvant regimens.

Significance: Multidimensional profiling of pretreatment esophageal adenocarcinoma shows patient response to nCT is correlated with active preexisting immunity and indicates molecular pathways of resistance that may be targeted to improve clinical outcomes.

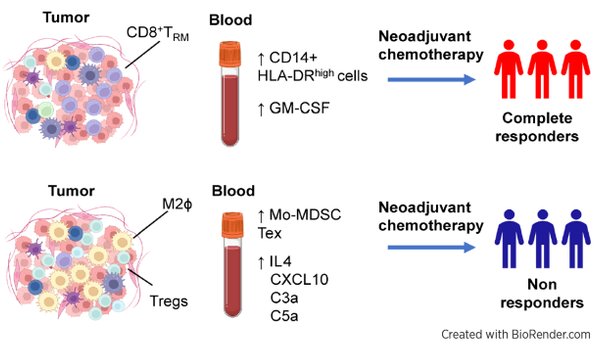

Introduction

Esophageal cancer is the sixth most common cause of global cancer-associated deaths worldwide (1). Esophageal adenocarcinoma (EAC), its pathologic variant, is the predominant subtype in Western countries, which have seen a sharp increase in its incidence over the past four decades (1). EAC typically affects the distal esophagus near the gastric junction; it is associated with obesity, gastroesophageal reflux, and a precursor condition known as Barrett's esophagus (1). EAC is characterized by high tumor mutational burden (TMB), large-scale chromosomal instability, and genomic structural alterations, which contribute to a poor prognosis with less than 20% of patients surviving beyond 5 years (1). Most patients with EAC are diagnosed with locally advanced disease, which invades local tissues or involves regional lymph nodes without distant metastases [American Joint Committee on Cancer (AJCC) stage ≥ T2 or N+, M0]. To reduce tumor bulk and improve survival, neoadjuvant (preoperative) chemotherapy (nCT), either alone or in combination with radiation therapy, is recommended for all locally advanced cases, followed by radical surgery (1–3). However, only about 30% of treated patients show a pathologic CR with tumor and/or lymph node downstaging, which is associated with a 5-year survival rate of 64% in complete responders

[1]Experimental Immunology Unit, IRCCS San Raffaele Scientific Institute, Milan, Italy. [2]Vita-Salute San Raffaele University, Milan, Italy. [3]Department of Pathology, IRCCS San Raffaele Scientific Institute, Milan, Italy. [4]Center for OMICS Sciences, IRCCS San Raffaele Scientific Institute, Milan, Italy. [5]Hematology and Bone Marrow Transplant Unit, IRCCS San Raffaele Scientific Institute, Milan, Italy. [6]Department of Gastrointestinal Surgery, IRCCS San Raffaele Scientific Institute, Milan, Italy. [7]Division of Gastroenterology & Gastrointestinal Endoscopy, San Raffaele Scientific Institute, Milan, Italy. [8]Department of Oncology, IRCCS San Raffaele Scientific Institute, Milan, Italy.

G. Casorati and P. Dellabona contributed equally to this article.

Corresponding Authors: Giuseppina Arbore, IRCCS San Raffaele Scientific Institute, Via Olgettina 58, Milan 20132, Italy, Phone: 392-2643-4735; E-mail: arbore.giuseppina@hsr.it; Paolo Dellabona, dellabona.paolo@hsr.it; and Giulia Casorati, casorati.giulia@hsr.it

Cancer Res 2023;83:2873–88

doi: 10.1158/0008-5472.CAN-23-0356

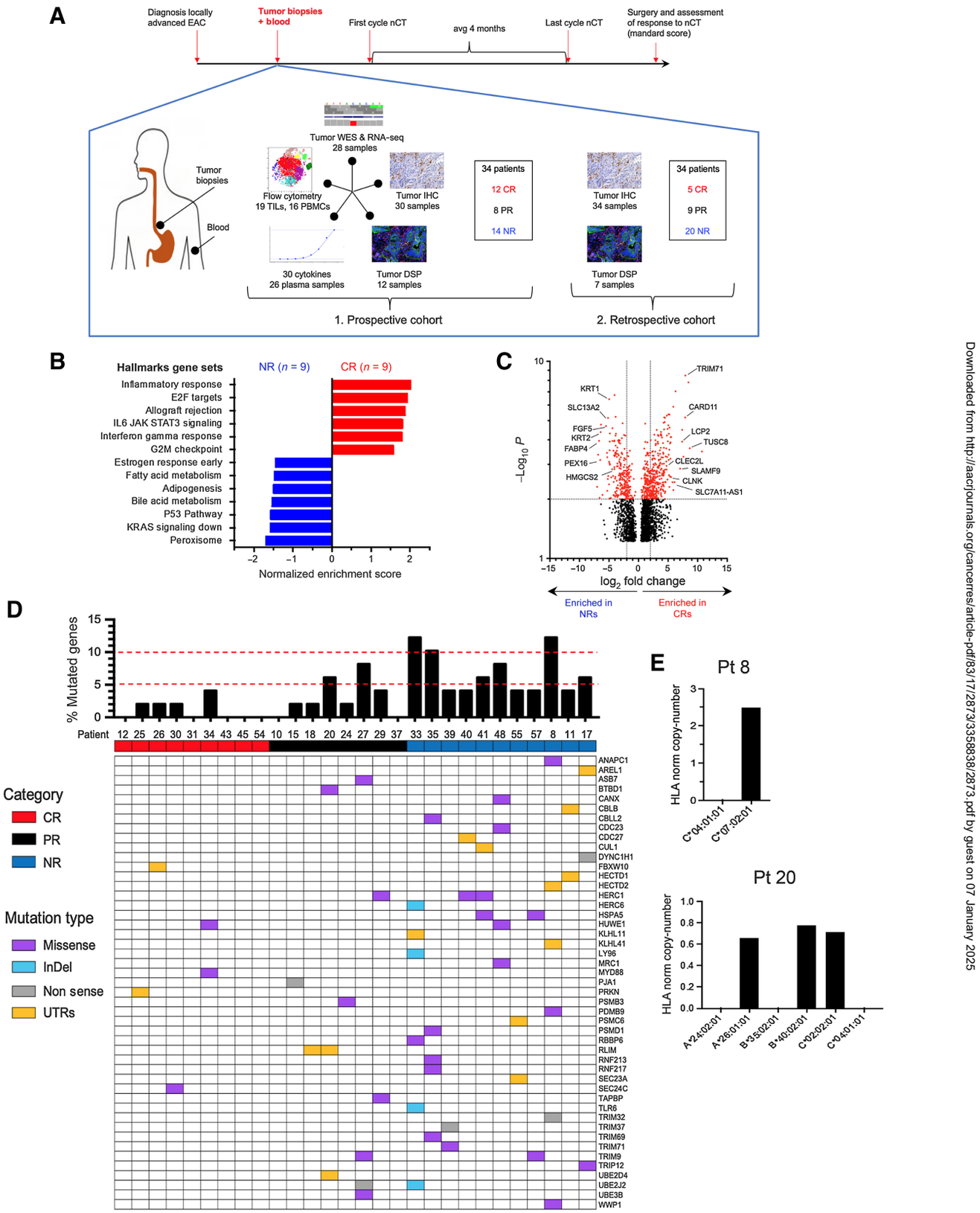

(CR) compared with 18% in nonresponders (NR; refs. 1–2). Nevertheless, the mechanisms underlying EAC response to nCT remain largely undefined. Consequently, identifying predictors of response could improve patient stratification and inform the design of more efficacious neoadjuvant and/or adjuvant therapies, which may increase response rates without subjecting patients to unnecessary treatments.

Effective cancer control depends on active immune surveillance, particularly by tumor-reactive T cells. The presence of tumor-infiltrating T lymphocytes (TIL) has also been associated with better prognosis in several malignancies (4). Nonsynonymous somatic DNA mutations in cancer cells generate unique tumor neoantigens that serve as strong targets for cancer-reactive T cells (5). However, tumor-specific T-cell immunity is often suppressed by several mechanisms that can be effectively targeted by therapies to restore efficient disease control. For instance, immunotherapy using mAb to block inhibitory immune checkpoint molecules has been successfully employed in reinstating T-cell functions (6). In addition, the efficacy of conventional chemotherapy and radiotherapy is not solely dependent on the direct effects of antineoplastic agents or radiation on cancer cells but also on the stimulation of the host immune system, which is ultimately responsible for eliminating the tumor and the ensuing long-lasting clinical effects (7, 8). Indeed, both the antineoplastic drugs (e.g., platinum derivatives, 5-fluorouracil, taxanes) and radiation utilized in nCT protocols for EAC are capable of inducing immunogenic cancer cell death, which, in turn, stimulates the tumor-specific immune response and/or has direct immunomodulatory effects (7–9).

Given these perspectives, it remains unknown whether the pathological CR attained by preoperative treatments in a subset of patients with EAC is driven by immunoreactive tumor microenvironment (TME), which stimulates the tumor-specific T lymphocyte response and contributes to cancer cell elimination. To examine this hypothesis, molecular and immune profiling of the TME in EAC needs to be performed to assess the baseline composition of the TME prior to therapy. However, there is a lack of such data in the literature. Thus, in this study, we performed deep multidimensional profiling of baseline (i.e., pretreatment) tumor biopsies and paired baseline blood samples to unravel the immune determinants that might contribute to the variability in treatment response to nCT.

Materials and Methods

Study design

All samples analyzed in this study were collected from patients with EAC diagnosed with a locally advanced tumor (AJCC stage ≥ T2 or N+, M0), who received treatment at San Raffaele Research Hospital (Milan, Italy) between 2014 and 2021. All samples were collected at baseline (i.e., before patients received treatment). The study leveraged prospective and retrospective patient cohorts (Supplementary Fig. S1). The Institutional Ethics Committee approved the prospective observational study (protocol ESO-CA001), which was conducted at San Raffaele Research Hospital (OSR) in Milan, Italy. The San Raffaele Hospital Oncology Board made therapy decisions based on patients' clinical condition and the current European Society for Medical Oncology (ESMO) Clinical Practice Guideline for esophageal cancer treatment (3). Written informed consent was obtained from all patients of the prospective cohort ($n = 34$; Supplementary Table S1), including the collection and analysis of endoscopy biopsies of tumor tissue (6–8 biopsies per patient) and blood samples (50 mL). Whole-exome sequencing (WES), bulk RNA sequencing (RNA-seq), IHC, digital spatial tissue profiling (DSP), and high-dimensional flow cytometry were performed to analyze tumor samples. Plasma was isolated from blood supernatant and frozen at −80°C, while peripheral blood mononuclear cells (PBMC) were obtained by Ficoll separation (Ficoll-Paque PLUS, GE Healthcare Bio Sciences). Pretreatment tumor biopsies were freshly frozen in optimal cutting temperature OCT ($n = 4$ biopsies per patient) for genomic analysis. For flow cytometry analysis, 2 to 4 EAC biopsies were dissociated in RPMI media (Gibco) using the GentleMACS (Miltenyi Biotec) Dissociator and human tumor dissociation kit. After surgery, two expert gastrointestinal pathologists, who were blinded to the clinical data, assessed the post-nCT pathological response status by examining surgical resections.

In addition to the prospective patient cohort, archived clinically annotated baseline EAC biopsies from a second independent retrospective cohort of patients were analyzed to increase the sample size for the IHC and DSP analyses. These samples were available at San Raffaele Hospital ($n = 34$; protocols DSAN 718/1F and DSAN 0565/5TF) and are detailed in Supplementary Table S2. The archived tumor material was formalin-fixed and paraffin-embedded (FFPE), making it suitable for tissue studies but unsuitable for transcriptional analysis due to insufficient RNA quality compared with freshly frozen prospectively collected tumor biopsies.

Both patient cohorts (Supplementary Tables S1 and S2) underwent nCT with platinum derivatives, alone or in combination with radiotherapy, mainly following the treatment protocols FLOT (combining the drugs fluorouracil, leucovorin, oxaliplatin, and docetaxel) and CROSS (combining the drugs carboplatin and paclitaxel with radiotherapy at 41.4 Gy given in 23 fractions). The studies were conducted in accordance with the Declaration of Helsinki and were approved by the San Raffaele Ethics Committee.

WES and RNA-seq

WES and RNA-seq were performed on treatment-naïve EACs. To mitigate the elevated heterogeneity described for EAC (1), 3 to 4 biopsies that sampled different areas of each tumor were pooled before being subjected to nucleic acid extraction. Next, freshly frozen EAC biopsies were sectioned for DNA and RNA extraction, while two adjacent sections were evaluated by hematoxylin and eosin staining to determine the tumor content (>70% for sequencing). Genomic DNA and total RNA were extracted using the AllPrep DNA/RNA extraction kit (Qiagen). Nucleic acid quantification and quality control were performed using the DNA ScreenTape system (Agilent). A detailed description of WES and RNA-seq data acquisition and analysis are reported in the Supplementary Materials and Methods.

Figure 1.

Baseline higher immune gene signatures and reduced resistance to stress are associated with response to nCT. **A,** Schematic overview of the study design showing our multidimensional analysis of pre-nCT tumor biopsies (WES, RNA-seq, IHC, proteome DSP, and flow cytometry analysis) and blood (flow cytometry analysis, plasma cytokines) collected prospectively from patients diagnosed with locally advanced EAC ($n = 34$); an additional cohort of archived pretreatment EAC tumors ($n = 34$) was analyzed by IHC and DSP. **B,** Hallmark GSEA comparison of CRs ($n = 9$) versus NRs ($n = 9$) showing normalized enrichment scores for gene sets with FDR < 0.01. **C,** Volcano plot of genes enriched in CRs versus NRs from bulk RNA-seq. The volcano plot reports the name of genes selected on the basis of their participation in pathways differentially enriched in GSEA analysis, as discussed in the Results section. **D,** Oncoplot of somatic mutations in Reactome pathway MHC class I antigen processing and presentation genes, with respective percentages of mutated genes for each EAC sample. **E,** HLA LOH events represented as imbalanced HLA copy numbers observed in two patients, N 20 (PR) and N 8 (NR).

Histological analysis

FFPE (4-μm–thick) sections from treatment-naïve endoscopy tumor biopsies of EAC cases diagnosed at San Raffaele Research Hospital between 2014 and 2021 were subjected to IHC. The histologic analysis included 30 samples from the prospective patients with EAC cohort (ESO-CA001) and 34 from the retrospective cohort (protocols DSAN 718/1F and DSAN 0565/5TF; Supplementary Fig. S1). The primary mAbs used for IHC are reported in Supplementary Table S3. Horseradish peroxidase–labeled goat anti-mouse and anti-rabbit IgGs (Zhongshan Golden Bridge Biotechnology) were used for IHC as secondary antibodies. Tumor and stromal protein expression was graded with a semiquantitative h score, ranging from 0 (no staining) to 3 (the strongest staining) based on the prevalence of positive cells. Two histopathologists blinded to the clinical data graded the protein expression.

GeoMX DSP

To perform DSP (NanoString, RRID:SCR_021660) on treatment-naïve EAC tissue sections, we first identified tumoral areas on the basis of the morphologic analysis of adjacent tissue sections stained with hematoxylin and eosin. Then, on the next tissue section, we performed immunofluorescence (IF) staining using customized monoclonal antibodies against pan-cytokeratin (PanCK), hCD3, and hCD68 as morphology markers and a customized multiplexed panel of protein antibodies ($n = 59$). The panel contained photocleavable indexing oligonucleotides, which enabled subsequent readouts.

Spatially nonadjacent regions of interest (ROI) were selected on a DSP prototype instrument based on immunofluorescent visualization of PanCK (tumor epithelia), CD3 (T lymphocytes), CD68 (macrophages), and DAPI (nuclei). Two custom segmentation masks were generated using PanCK IF for separate analysis of $PanCK^+$ (cancer epithelia) and $PanCK^-$ (immune-infiltrated stromal) regions. Ultraviolet light was used to illuminate each segmented ROI, and indexing oligonucleotides were released from each segment. They were then collected and deposited into designated wells on a microtiter plate, allowing for well-indexing of each ROI and direct readout of protein hybridization. For each tissue sample, marker counts were obtained from an average of 4 (range 1–7) PanCK-negative versus PanCK-positive ROIs. For each marker, raw protein counts per ROI were generated using nCounter45 (nCounter MAX system version 4.0.0.3) and normalized to External RNA Control Consortium controls based on the geometric mean of three positive control markers. To measure total protein density, DSP reads were normalized to the ROI area. The DSP analysis suite (NanoString Technologies) was used for correlation, tSNE, Volcano, and box plots. Statistical analysis of Volcano plots was performed using a linear mixed model.

Flow cytometry

PBMCs or tumor cell suspensions were incubated in phosphate-buffered saline solution (PBS) with 2% fetal bovine serum (FBS) for 15 minutes in Fc Blocker (BD Biosciences, catalog no. 564220). Afterward, the cells were stained for 20 minutes with mAb panels. To investigate TILs obtained from six biopsies, a mAb panel 2 ($n = 20$ mAbs) directed against 20 surface markers (Supplementary Table S4) was used. This panel was used to stain the same TILs that were previously analyzed with the small T regulatory cells (Treg)/Teff panel (CRs $n = 3$, NRs $n = 3$; Supplementary Fig. S1). A second independent panel of 10 mAbs, detecting key subset-specific surface markers and five intracellular transcription factors associated with specific T-cell functions (mAb panel N3; Supplementary Table S4), was used to stain TILs obtained from six different baseline EAC biopsies that had not been stained with any previous panel (CRs $n = 3$, NRs $n = 3$; Supplementary Fig. S1).

For intracellular/intranuclear staining (panel 3), cells were fixed/permeabilized using the FOXP3/Transcription Factor Staining Kit (eBioscience). The cells were acquired on the BD FACSCanto II (panel 1), BD FACSymphony (panels 2 and 4), or BeckmanCoulter CytoflexLX (panel 3), and analyzed using FlowJo software (Beckton Dickinson, RRID:SCR_008520). Dead cells were identified and excluded by staining with DAPI or using the Live/Dead Fixable Blue Dead Cell Stain Kit (Invitrogen, catalog no. L23105) upon fixation. The relative fluorescence intensity was calculated from the mean fluorescence intensity (MFI) of the negative control (cluster negative for marker expression) within the corresponding gate. For high-dimensional analysis, flow cytometry standard data were exported from FlowJo after gating of lymphocytes, singlets, and viable $CD45^+$ cells. The t-distributed stochastic neighbor embedding (t-SNE) maps were built after sample dimensionality reduction to 3,000 events, and the PhenoGraph algorithm (https://github.com/jacoblevine/PhenoGraph, RRID:SCR_016919) was applied for cell clustering. The fluorescence intensity of all markers was exported into FlowJo to calculate the cell frequency per cluster and MFI per cluster for each fluorochrome, and samples from CRs and NRs were compared.

Plasma cytokine measurement

To assess 27 cytokines, we used the Bio-Plex Pro-Human 27-plex Assay and followed the manufacturer's instructions. The readouts were obtained using the Bioplex200 machine and Bio-Plex Manager 6.0 software (Bio-Rad). ELISA was performed using the Complement C3a Human ELISA Kit (Invitrogen, BMS2089), Complement C5a Human ELISA Kit (Invitrogen, BMS2088), and VeriKine-HS Human Interferon Beta Serum ELISA Kit (PBL Assay Science, PBL-41415–1).

Statistical analysis

Statistical analysis was performed using GraphPad Prism 8.0 (GraphPad Software, RRID:SCR_002798). Differences between groups were assessed with two-tailed unpaired t tests or Wilcoxon tests, unless otherwise specified. Linear correlations between two parameter categories were evaluated using Spearman rank-order correlation. For multiple group comparisons, ANOVA was performed. A $P < 0.05$ was considered statistically significant. Overall survival (OS) was defined as the time interval between initial surgical excision and death or the last follow-up (censored). Disease survival was defined as the time interval between initial surgical excision and diagnosis of metastasis/disease progression or the last follow-up. Kaplan–Meier plots were constructed using GraphPad Prism software (RRID: SCR_002798) and analyzed using the log-rank test.

Data availability

The data generated in this study are available upon request from the corresponding author. WES and RNA-seq data are deposited into the European Genome-phenome Archive (EGA) public repository, accession number EGAS00001007245.

Results

Participants, samples, and study design

To compare the preexisting TME in patients with EAC showing variable response to preoperative therapies, we prospectively collected paired blood and endoscopic bioptic tumor samples from patients ($n = 34$) at baseline (i.e., before neoadjuvant therapy; **Fig. 1A**). Subsequently, the recruited patients underwent nCT alone or in

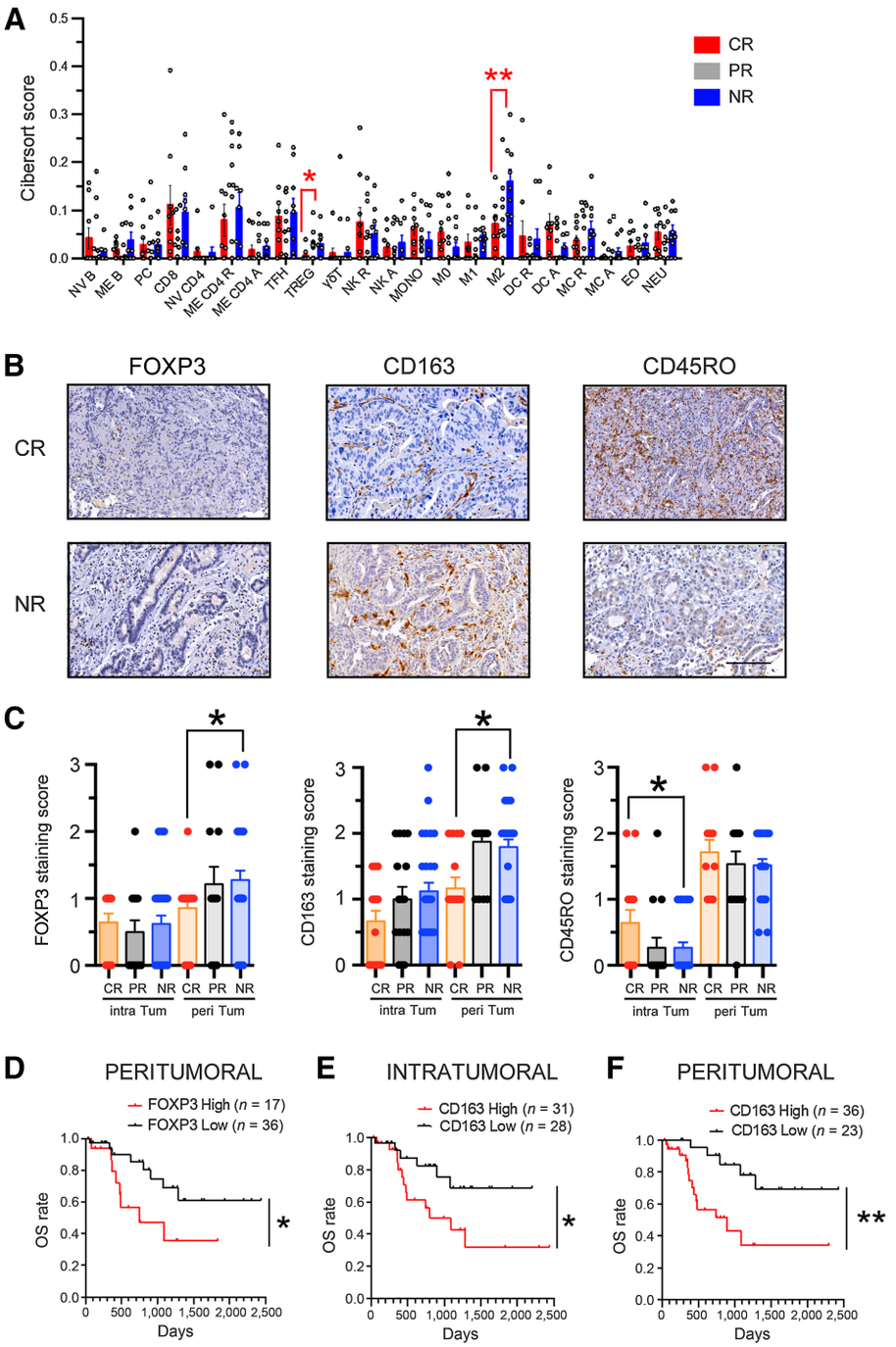

Figure 2.

Increased baseline infiltration of FOXP3$^+$ and CD163$^+$ cells in EACs of NRs is associated with reduced OS. **A,** CIBERSORT scores for EAC-infiltrating immune cell populations were calculated from RNA-seq data for CRs, PRs, and NRs. Bar graphs represent mean ± SEM. *, $P<0.05$; **, $P<0.01$; one-way ANOVA. NV B, naïve B; ME B, memory B; P, plasma cells; CD8, CD8$^+$; NV CD4, naïve CD4$^+$; ME CD4 R, memory CD4$^+$ resting; ME CD4 A, memory CD4$^+$ activated; TFH, follicular T helper; γδT, gamma delta T; NK R, natural killer resting; NK A, natural killer activated; MONO, monocytes; M0, M0 macrophages; M1, M1 macrophages; M2, M2 macrophages; DC R, dendritic cells resting; DC A, dendritic cells activated; MC R, mast cells resting; MC A, mast cells activated; EO, eosinophils; NEU, neutrophils. **B,** Representative immunostaining of pretreatment EACs for FOXP3, CD163, and CD45RO. Scale bar, 50 μm. **C,** Staining scores for intratumoral (intra Tum) and peritumoral regions (peri Tum) in CRs ($n = 15$), PRs ($n = 16$), and NRs ($n = 33$). Semiquantitative h scores (0 = no staining to 3 = strongest staining) were assigned by an expert pathologist. Data are presented as mean ± SEM. *, $P<0.05$; one-way ANOVA. **D,** OS of patients with high versus low FOXP3 IHC staining scores in intratumor EAC infiltrates before neoadjuvant chemotherapy (high score, h ≥ 1; low score, h < 1). *, $P<0.05$; log-rank test. **E** and **F**, OS of patients with high versus low CD163 IHC staining scores in peritumoral (**E**) and intratumoral (**F**) EAC infiltrates before neoadjuvant chemotherapy (high score, h ≥ 2; low score, h < 2). *, $P < 0.05$; **, $P < 0.01$; log-rank test.

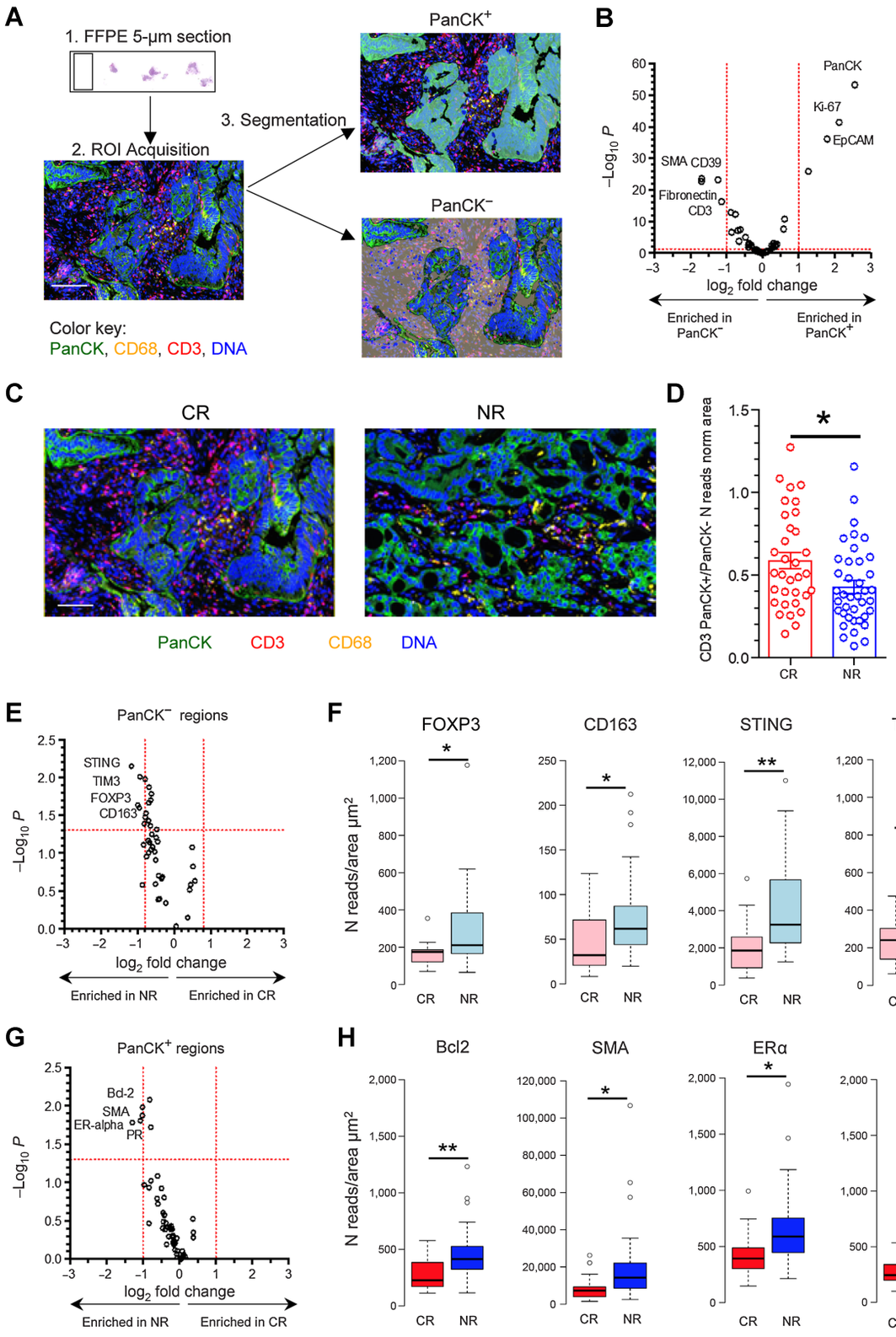

combination with radiotherapy (Supplementary Table S1). All nCT treatment schemes utilized platinum derivative compounds that were mechanistically correlated in terms of their immunomodulatory properties (7, 9). After completing nCT, patients underwent surgery, and the degree of pathologic response to treatment was assessed in their resected tumors with the Mandard tumor regression score (TRG; ref. 10). Patients were subdivided into CRs ($n = 12$, TRG1–2), partial responders (PR; $n = 8$, TRG3), and NRs ($n = 14$, TRG4–5). Although not statistically significant, likely due to the small sample size, CRs showed a better 5-year survival trend compared with PRs and NRs (Supplementary Fig. S2A), which was consistent with previous clinical studies (11). Further, the banked baseline tumor and blood samples collected from this prospective cohort were subjected to a multidimensional analysis, for which different methods were employed depending on sample characteristics (**Fig. 1A**; Supplementary Fig. S1). To increase the sample size for IHC and DSP analyses, we added archived clinically annotated baseline EAC biopsies from a second independent retrospective cohort of patients available at San Raffaele Hospital (Supplementary Table S2, Supplementary Fig. S1), combining them with the samples from the prospective patient cohort. All findings presented in this report refer to the baseline characteristics of tumors before nCT.

Baseline higher immune gene signatures and reduced resistance to stress are associated with response to nCT

We performed WES and RNA-seq of 26 baseline EAC samples that passed DNA and RNA quality check; two additional EAC samples were subjected to WES only (Supplementary Fig. S1). Gene set enrichment analysis (GSEA) of the RNA-seq data revealed significant enrichment of hallmark gene sets related to immune response, type I inflammation, and proliferation in CR versus NR tumors (**Fig. 1B**), suggesting an overall association between nCT response and active immune infiltration, increased cell proliferation, and chemo/chemoradiation vulnerability. EACs of CRs showed significantly higher expression of genes associated with functions consistent with the GSEA pathways, including suppression of tumorigenesis (*TRIM71*; ref. 12), promotion of T-cell receptor signaling and intratumor T-cell infiltration (*CLNK, LCP2/SLP-76*; refs. 13, 14), immunoinflammatory response (*SLAMF9*; ref. 15), suppression of migration (*CLEC2L, CARD11, TUSC8*; refs. 16, 17), chemotherapy response, and susceptibility to immunogenic cancer cell death ferroptosis (*SLC7A11-AS1*; **Fig. 1C**; refs. 18, 19). In contrast, EACs of NRs revealed significantly enriched pathways associated with resistance to stress, oncogenic activation, peroxisomal function, fatty acid metabolism, and estrogen response (**Fig. 1B**). Notably, the P53 pathway, KRAS signaling downregulated genes, and early estrogen response pathways are known to be associated with the progression of malignant melanoma (20). Baseline EACs of NRs showed significantly higher expression of genes involved in tumor invasion (*FGF5*, cytokeratin *KRT1*, and cytokeratin *KRT2*; refs. 21, 22), oxidative metabolism (*SLC13A2, HMGCS2*; ref. 23), lipid synthesis (*FABP4*; ref. 24), and peroxisomal function (*PEX16*; ref. 25), which is consistent with these hallmarks (**Fig. 1C**). Although EAC cases showing partial response to nCT represent a prognostically heterogeneous cohort (residual tumor cells between 10% and 50% in the surgical resection; refs. 10, 26), hallmark GSEA confirmed the upregulation of the same molecular pathways that were differentially expressed in NRs versus CRs (Supplementary Fig. S2B).

We did not observe significant differences in overall TMB, which affects the probability of the formation of tumor neoantigens that TILs may recognize (5). Similarly, no significant differences were seen in tumor neoantigen load between CR and NR tumors (Supplementary Fig. S2C and S2D). This contrasts with the results of previous reports (26), likely due to the smaller sample size of our study (9 CRs vs. 9 NRs). However, compared with CRs and PRs, baseline tumors of NRs exhibited a significantly higher mutational load in genes of the Reactome pathway MHC class I antigen processing and presentation (**Fig. 1D** and Supplementary Fig. S2E, Supplementary Table S5). There were no significant differences in mutational load in EAC driver genes (Supplementary Fig. S2F and S2G, Supplementary Table S6). Alterations in the presentation of MHC class I antigens are associated with a worse prognosis of several malignancies (27) and may negatively impact the antitumor immune response in EAC. In our sample, only one NR and one PR case demonstrated loss of heterozygosity of HLA class I alleles (**Fig. 1E**), another factor correlated with reduced likelihood of MHC class I antigen presentation (28).

Collectively, these results suggest that response to nCT was dependent on preexisting active immune infiltration and higher susceptibility to chemotherapy and radiotherapy in the responding tumors. On the other hand, nonresponding tumors were characterized by increased immunosuppression and resistance to oxidative stress.

Distinct baseline patterns of myelomonocytic and T-cell infiltration distinguish responders from NRs to nCT

To better understand the differences in immune contextures between CRs and NRs, as suggested by the genomic analysis, we used the CIBERSORT tool to estimate the immune composition of the tumor biopsies from bulk RNA-seq data. Our analysis revealed significantly reduced signatures for immunosuppressive Tregs and M2-like macrophages in CRs compared with NRs (**Fig. 2A**).

We then performed IHC of specific immune cell markers to confirm the differential tumor infiltration of immunosuppressive Tregs and M2-like macrophages between CRs and NRs and subsequently examine potential antitumor effector T cells. We stained sections of 30 prospectively collected baseline EAC biopsies with markers for Treg (FOXP3), M2-like macrophage (CD163), and effector memory T cells (CD45RO; **Fig. 2B**). The results showed that NRs exhibited a trend toward increased peritumoral FOXP3 and CD163 staining, while CRs showed higher levels of intratumoral CD45RO staining (Supplementary Fig. S3A). To validate these findings, we stained baseline EAC biopsies from an independent retrospective archived cohort ($n = 34$ cases) and confirmed significantly higher levels of staining for CD163 in NRs compared with

Figure 3.

DSP confirms distinct baseline functional immune contexture in EACs of CRs and NRs. **A,** Experimental design: spatial proteomic profiling of 53 tumor and immune markers was conducted on FFPE EAC biopsy sections; selection of multiple ROIs per tissue sample was based on immunofluorescent staining for PanCK (tumor epithelial marker), CD68 (macrophages), and CD3 (T lymphocytes); nuclei were stained with 4',6-diamidino-2-phenylindole (DAPI). Protein counts were measured within PanCK$^+$-enriched tumor regions (masks) and PanCK$^-$ stromal regions (inverted masks). **B,** Volcano plot of proteins enriched in PanCK$^+$ ($n = 72$) versus PanCK$^-$ ($n = 72$) areas showing statistical significance for proteins with $P < 0.05$; P values were calculated using the linear mixed model. **C,** Representative immunofluorescent staining for PanCK, CD68, and CD3 in tumor tissue from CRs and NRs. Scale bar, 100 μm. **D,** CD3 PanCK$^+$/PanCK$^-$ ratios for each ROI (normalized by area) for CRs and NRs (calculated from DSP reads). *, $P < 0.05$, unpaired t test. **E** and **G,** Volcano plots of proteins enriched in PanCK$^-$ (**E**) and PanCK$^+$ (**G**) areas in tumors from CRs ($n = 33$ ROIs) versus NRs ($n = 39$ ROIs), showing statistical significance for proteins with $P < 0.05$; P values were calculated using the linear mixed model. **F** and **H,** Corresponding box plots representing read numbers (N) normalized to the area for proteins differentially enriched in PanCK$^-$ (**F**) and PanCK$^+$ areas (**H**), presented as mean ± SEM. *, $P < 0.05$; **, $P < 0.01$, unpaired t test.

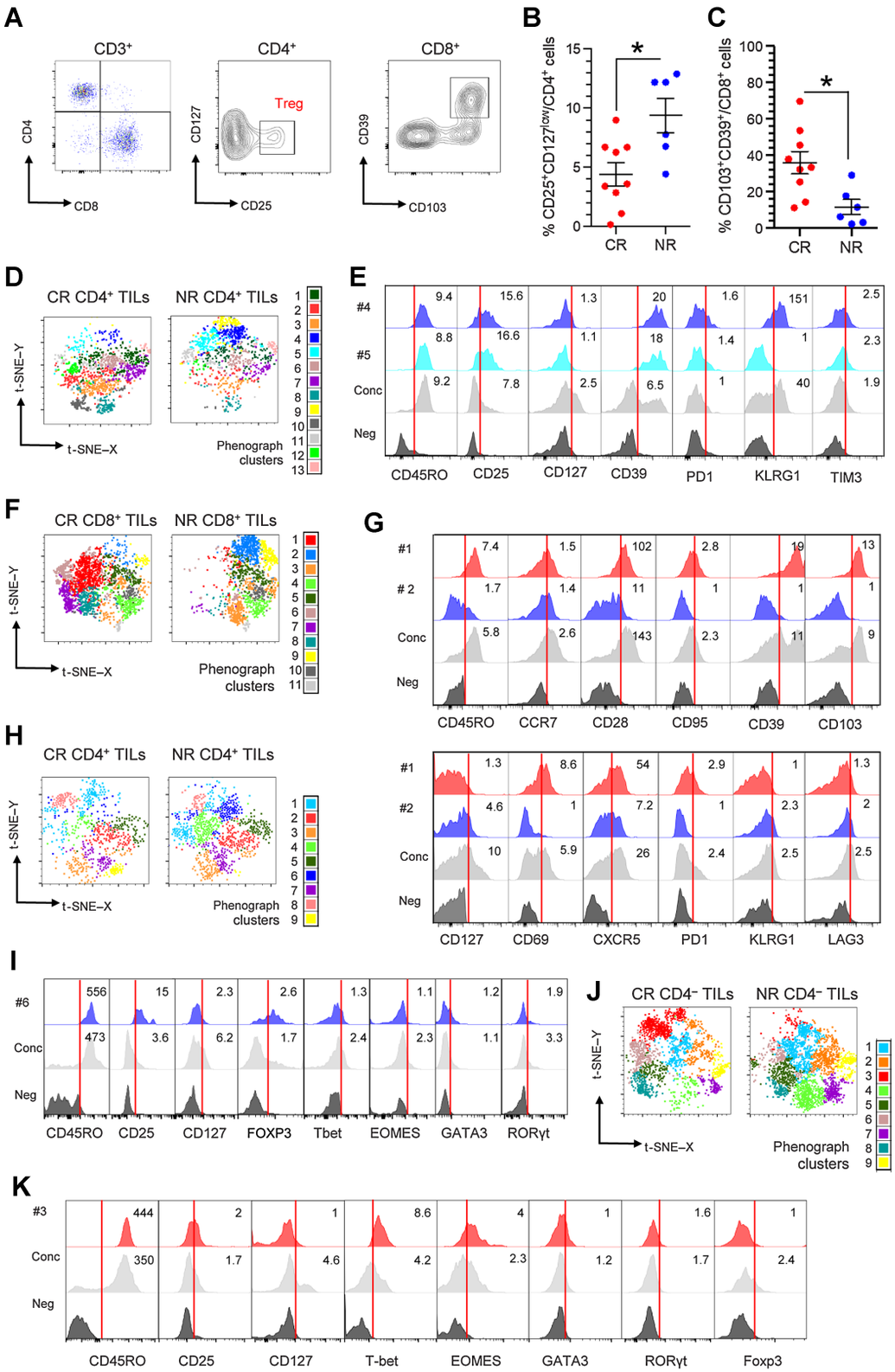

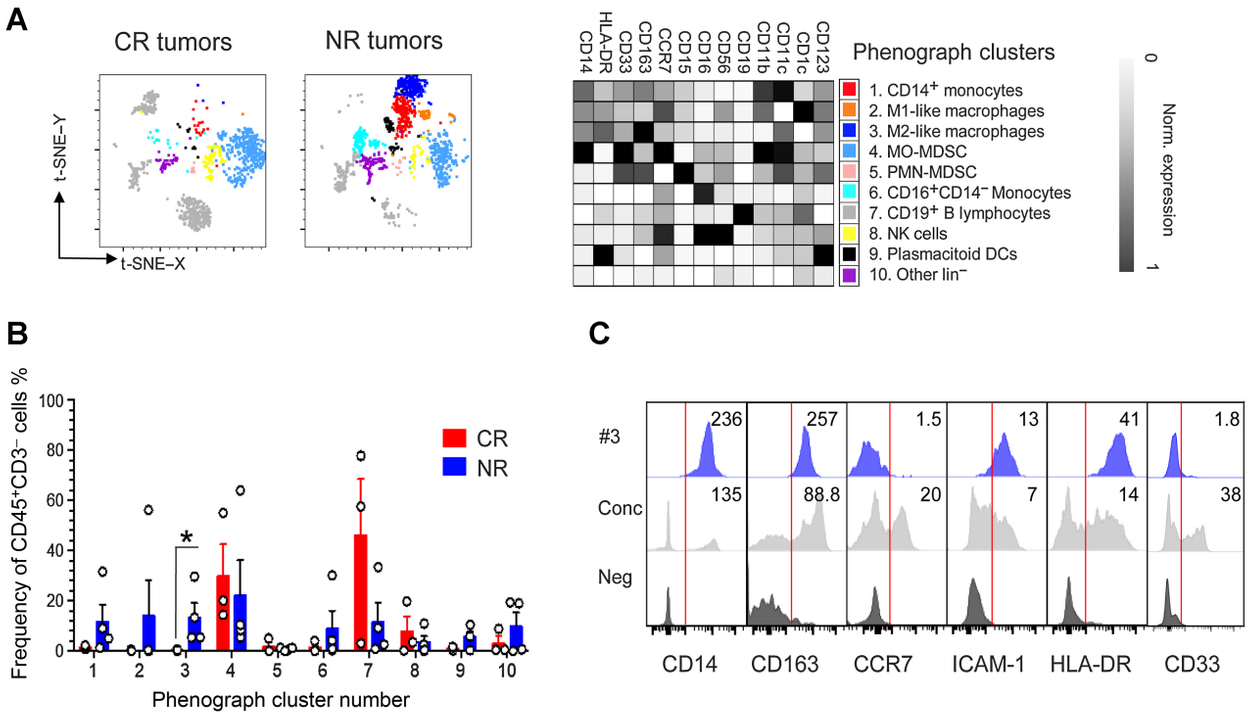

Figure 5.

NR EACs show increased baseline infiltration of protumor M2-like macrophages. **A,** Exemplified tSNE visualization of 20 surface markers representing 7,000 merged CD45$^+$ CD3$^-$ tumor cells from CRs ($n = 3$) and NRs ($n = 4$); cells are colored according to the 10 clusters assigned by PhenoGraph and manual annotation; the corresponding heatmap shows median marker intensity normalized to a 0 to 1 range. **B,** Frequencies of the clusters in CR ($n = 3$) and NR ($n = 4$) CD45$^+$ CD3$^-$ cells presented as mean ± SEM. *, $P < 0.05$; one-way ANOVA. **C,** Histograms showing the expression of six surface markers in cluster #3 (assigned as M2-like macrophages), concatenated CD45$^+$ CD3$^-$ events (Conc), and negative control (Neg) relative fluorescence intensity (RFI) values are shown.

CRs (Supplementary Fig. S3B). We also confirmed the trend for increased FOXP3 and decreased CD45RO in baseline EAC biopsies. By combining data from the two cohorts, we further confirmed higher levels of "immunoregulatory" FOXP3 and CD163 expression in NRs compared with CRs, which was statistically significant (**Fig. 2C**). In addition, we observed higher levels of CD45RO in CRs, indicating enrichment for intratumoral effector memory cells (**Fig. 2C**). Moreover, a trend for higher peritumoral staining scores for FOXP3 and CD163 and for lower intratumoral staining scores for CD45RO was still present in each separate group of NRs who received either combined nCT and radiotherapy (nCT + RT) or nCT alone, indicating a common underlying immune mechanism associated with treatment response to both neoadjuvant regimens (Supplementary Fig. S3C and S3D). No significant differences in the levels of CD3, CD4, CD8, or the pan-macrophage marker CD68 were detected (Supplementary Fig. S4A and S4B). Remarkably, higher levels (h ≥ 2) of peritumoral FOXP3 staining and CD163 immunostaining were associated with reduced OS in the two combined cohorts of patients with EAC (**Fig. 2D–F**).

DSP supports differential baseline tumor immune infiltration in CRs and NRs

To enhance the tissue analysis with spatial resolution information, we conducted multiplex proteomic analysis using DSP on baseline EACs. Tumor sections were stained with 53 mAbs to detect functional

Figure 4.

Responder EACs show reduced baseline infiltration of FOXP3$^+$ Tregs and an increased frequency of tissue-resident CD8$^+$CD39$^+$ T cells. **A,** Representative flow cytometry plots of tumor single-cell suspensions (CD3$^+$ viable cells) stained for nine surface markers, showing the gating strategy for CD25$^+$ CD127^{low} Tregs and CD8$^+$ CD39$^+$ CD103$^+$ T cells. **B** and **C,** Dot plots showing frequencies expressed as percentage of CD25$^+$ CD127^{low} CD4$^+$ cells (**B**) and CD39$^+$ CD103$^+$ CD8$^+$ cells (**C**) in pretreatment EAC tumor cell suspensions from CRs ($n = 9$) and NRs ($n = 6$), determined by manual gating. Data are presented as mean ± SEM. *, $P < 0.05$, unpaired *t* test. **D,** Exemplified t-SNE visualization of 17 surface markers representing 6,000 merged CD3$^+$ CD4$^+$ cells in tumor cell suspensions from CRs ($n = 3$) and NRs ($n = 3$); 13 clusters were predicted by unsupervised PhenoGraph analysis. **E,** Histograms showing the expression of six surface markers in clusters #4 and #5, concatenated CD3$^+$ CD4$^+$ events (Conc), and negative control (Neg); relative fluorescence intensity (RFI) values are shown. **F,** Exemplified t-SNE visualization of 17 surface markers representing 6,000 merged CD3$^+$ CD8$^+$ cells in tumor cell suspensions from CRs ($n = 3$) and NRs ($n = 3$); 11 clusters were predicted by unsupervised PhenoGraph analysis. **G,** Histograms showing the expression (RFI values) of 12 surface markers in clusters #1 and #2, concatenated CD3$^+$ CD8$^+$ events, and negative control. **H,** Exemplified t-SNE visualization of eight markers, including three surface markers and five nuclear transcription factors, representing 6,000 merged CD3$^+$ CD4$^+$ cells in tumor cell suspensions from CRs ($n = 3$) and NRs ($n = 3$); nine clusters were predicted by unsupervised PhenoGraph analysis. **I,** Histograms showing the expression (RFI values) of seven markers in cluster #6, (CD25$^+$ CD127^{low} FOXP3$^+$ Treg-like cells), concatenated CD3$^+$ CD4$^+$ events, and negative control. **J,** Exemplified t-SNE visualization of 8 markers (three surface markers and five nuclear transcription factors), representing 6,000 merged CD3$^+$ CD4$^-$ cells in tumor cell suspensions from CRs ($n = 3$) and NRs ($n = 3$); nine clusters were predicted by unsupervised PhenoGraph analysis. **K,** Histograms showing the expression (RFI values) of eight markers in cluster #3, concatenated CD3$^+$ CD4$^-$ events, and negative control.

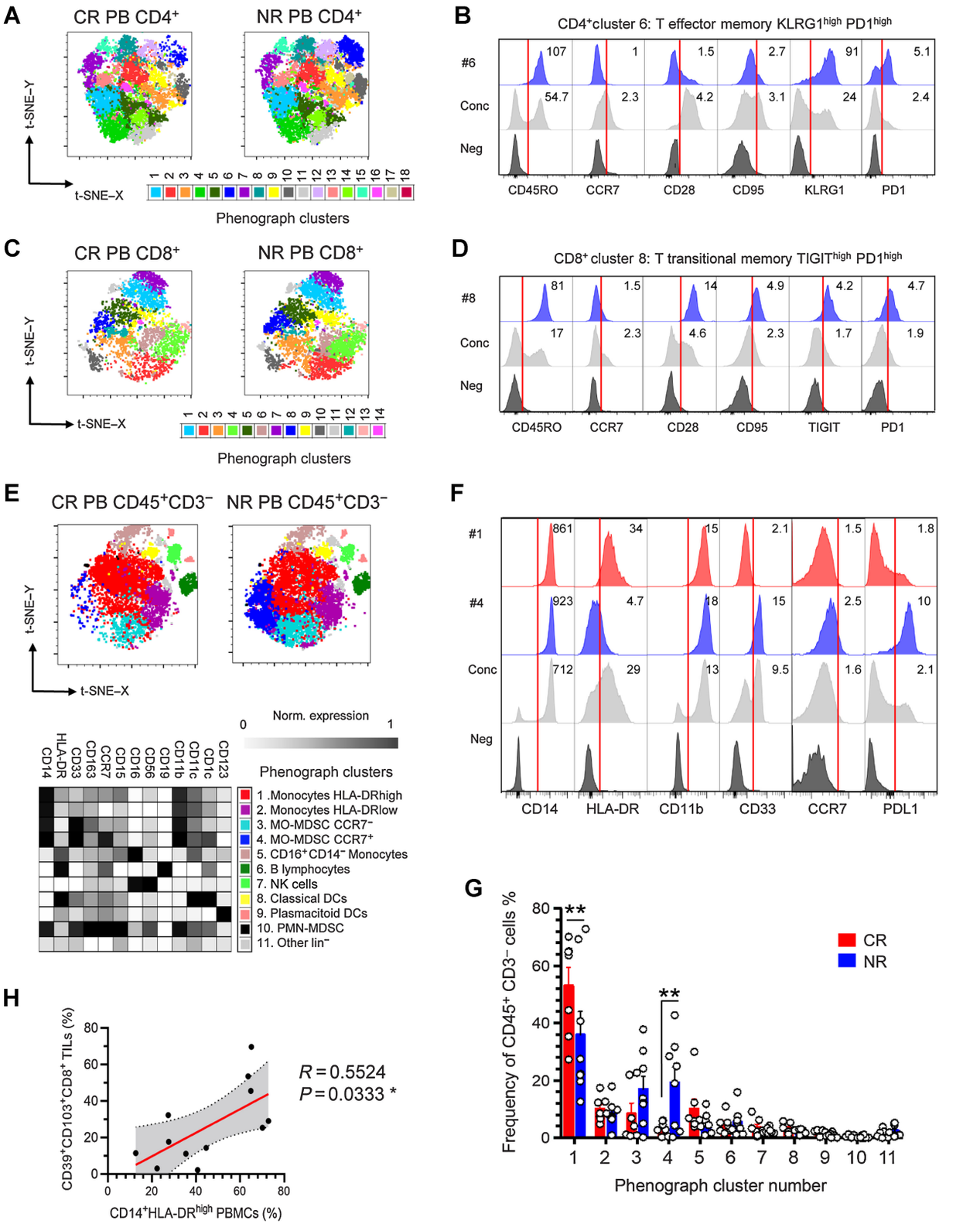

immune markers or proteins involved in known cell functions, followed by the analysis of selected ROIs (**Fig. 3A**). DSP for 53 tumor and immune proteins was performed on 144 regions of tumor sections obtained from 2 to 4 pooled EAC biopsies for each of the CR ($n = 9$) and NR ($n = 10$) tumors. Spatially separated ROIs were selected by visualizing the markers PanCK (tumor epithelia), CD3 (T lymphocytes), CD68 (macrophages), and DAPI (nuclei) using IF. PanCK$^+$ cancer epithelial regions were compared with PanCK$^-$ immune-infiltrated stromal regions (**Fig. 3A** and **B**; Supplementary Fig. S5A–S5F). We found significantly higher expression of the epithelial markers PanCK and EpCAM in PanCK$^+$ cancer cell areas, in contrast to the increased expression of the stromal markers alpha smooth muscle actin (SMA) and fibronectin and the lymphocytic markers CD3 and CD39 in PanCK$^-$ stromal regions (**Fig. 3B**). The ratios of the CD3 signal in PanCK$^+$ areas to the CD3 signal in PanCK$^-$ areas were significantly higher in the ROIs of CRs compared with NRs (**Fig. 3C** and **D**). This finding suggests a higher frequency of tumor-infiltrating T cells in EACs of CRs, indicating a possible correlation with the antitumoral immune response. Furthermore, PanCK$^-$ areas showed enrichment for FOXP3 and CD163 protein expression in NRs, indicating significantly increased infiltration by immunosuppressive Tregs and M2-like macrophages, which was consistent with our IHC data. The immune checkpoint molecule TIM3 and inflammation-related signaling mediator stimulator of IFN genes (STING) were also enriched in NRs (**Fig. 3E** and **F**). In addition, within the PanCK$^+$ cancer cell areas of NR tumors, there were significantly elevated levels of the antiapoptotic protein Bcl2 (associated with tumor survival; ref. 29), αSMA (associated with invasion and metastasis in gastric cancer; ref. 30), and the estrogen receptor alpha and progesterone receptor (correlated with prognosis of EAC and gastric cancer; **Fig. 3G** and **H**; refs. 31, 32).

Together, the spatially resolved tissue proteomics results provided additional evidence to support the characterization of a highly immunoreactive tumor infiltrate in baseline tumors of CRs, in contrast to an actively immunosuppressive and therapy-resistant infiltrate in tumors of NRs. This analysis also highlighted additional protein markers associated with the absence of a pathological response to nCT that could be further explored as potential therapeutic targets.

Distinct myelomonocytic and T-cell populations in baseline tumors of CRs versus NRs to nCT

To examine the differentially infiltrating EAC immune populations in greater detail, we used flow cytometry analysis to characterize TILs from 15 baseline tumor biopsies in the prospective cohort (Supplementary Fig. S1) using a panel of 7 mAbs detecting Treg and effector T cells (mAb panel N1, Supplementary Table S4). This analysis confirmed the significant enrichment of cells expressing a putative Treg phenotype in NR tumors (CD25$^+$CD127^{low}CD4$^+$; **Fig. 4A** and **B**), whereas CR tumors were characterized by a higher frequency of tissue-resident memory CD39$^+$CD103$^+$CD8$^+$ T cells (**Fig. 4A** and **C**), a population of cells often enriched in other solid tumors (33). We further deep-profiled the functional phenotype of TILs in baseline EAC biopsies using high-dimensional flow cytometry analysis with two complementary mAb panels (panels N2 and N3; Supplementary Table S4; Supplementary Fig. S6A–S6C). In NRs, unsupervised high-dimensional analysis of CD4$^+$ TILs highlighted a significantly increased frequency of putative CD25$^+$CD127^{low}CD39$^+$PD-1$^+$TIM3$^+$ Treg cells found in two clusters (#4 and #5; **Fig. 4D** and **E**; Supplementary Fig. S7A and S7C), differentiated by the expression of KLRG1. The increased frequency of TIM3$^+$ Tregs in TILs of NRs was consistent with the previous DSP data, which showed higher levels of TIM3 protein in baseline tumor biopsies of NRs. In addition, a third cluster of CD4$^+$ TILs (#9) containing putative exhausted CD39$^+$ LAG3$^+$ CD28$^-$ T effector memory cells (Supplementary Fig. S7A and S7C) showed their preferential accumulation in NRs. Furthermore, unsupervised clustering analysis of CD8$^+$ TILs in NRs revealed a highly enriched cluster (#2) displaying a CD103$^-$ CD69$^-$ CD45RO$^-$ CCR7$^-$ CD28$^-$ KLRG1$^+$ LAG3$^+$ phenotype, highly suggestive of exhausted and terminally differentiated nontissue-resident effector cells (**Fig. 4F** and **G**; Supplementary Fig. S8A and S8C). In contrast, CRs were characterized by an enriched population (#1) of tissue-resident memory CD45RO$^+$ CD39$^+$ CD103$^+$ CD69$^+$ CCR7$^-$ T cells that coexpressed CD28, CXCR5, and the exhaustion marker PD-1, but were negative for CD127 and all tested inhibitory receptors (**Fig. 4F** and **G**; Supplementary Fig. S8A and S8C). This population of cells is similar to an early dysfunctional tissue-resident CXCR5$^+$ CD8$^+$ T-cell subset that sustains effector responses in different cancers and chronic viral infections, and that is positively associated with response to anti–PD-1 immunotherapy (34, 35). The flow cytometric assessment of nuclear transcription factors expressed in CD4$^+$ T cells confirmed the accumulation of CD25^{high} CD127^{low} FOXP3$^+$ Tregs (#6) in tumors of NRs, with no significant differences in the expression of other transcription factors (**Fig. 4H** and **I**; Supplementary Fig. S7B and S7D). The analysis of nuclear transcription factors expressed in putative CD8$^+$effector/memory TILs (CD45RO$^+$ CD4$^-$ cells) showed an increased frequency of T-bet^{high}EOMES$^+$ cells (subset #3) in CRs (**Fig. 4J** and **K**; Supplementary Fig. S8B and S8D), reminiscent of early exhausted tumor-infiltrating cells found to sustain antitumor or chronic antiviral responses (35).

The myeloid cell composition of baseline tumor biopsies was also characterized by high-dimensional flow cytometric analysis of 22 extracellular markers (mAb panel N4; Supplementary Table S4; Supplementary Fig. S9). Unsupervised cluster analysis of the myeloid cell staining identified 10 populations (**Fig. 5A**), with only M2-like macrophages (#3, CD14$^+$ CD163$^+$ ICAM-1$^+$ HLA-DR^{high} CD33$^-$) being

Figure 6.

Increased frequency of circulating exhausted T cells and myeloid-derived suppressor MDSC cells in NRs to nCT prior to treatment. **A,** Exemplified t-SNE visualization of 17 surface markers representing 32,000 merged CD3$^+$ CD4$^+$ cells PBMCs from CRs ($n = 8$) and NRs ($n = 8$) before nCT; 18 clusters were predicted by unsupervised PhenoGraph analysis. **B,** Histograms showing the expression of six markers in cluster #6 (T effector memory KLRG1^{high} PD-1^{high}), concatenated CD3$^+$ CD4$^+$ events (Conc), and negative control (Neg); relative fluorescence intensity (RFI) values are shown. **C,** Exemplified t-SNE visualization of 17 surface markers representing 16,000 merged CD3$^+$CD8$^+$ pre-nCT PBMCs from CRs ($n = 8$) and NRs ($n = 8$); 14 clusters were predicted by unsupervised PhenoGraph analysis. **D,** Histograms showing the expression (RFI values) of six markers in cluster #8 (T transitional memory TIGIT^{high} PD-1^{high}), concatenated CD3$^+$ CD8$^+$ events (Conc), and negative control (Neg). **E,** Exemplified t-SNE visualization of 20 surface markers representing 15,000 merged CD45$^+$ CD3$^-$ pre-nCT PBMCs from CRs ($n = 7$) and NRs ($n = 8$). Cells are colored according to the 11 clusters assigned by PhenoGraph and manual annotation; the corresponding heat map shows median marker intensity normalized to a 0 to 1 range. **F,** Histograms showing the expression (RFI values) of five surface markers in PhenoGraph clusters #1 and #4, concatenated CD45$^+$ CD3$^-$ events, and Neg; clusters #1 and #4 were assigned as monocytes HLA-DR^{high} (enriched in CRs) and MO-MDSC CCR7$^+$ (enriched in NRs), respectively. **G,** Frequencies of CD45$^+$CD3$^-$ cells in 11 PhenoGraph clusters (determined by 20 surface markers) in CRs ($n = 7$) and NRs ($n = 8$), presented as mean ± SEM. **, $P < 0.01$; one-way ANOVA. **H,** Correlation between the flow cytometry frequency (%) of CD14$^+$HLA-DR^{high} PBMCs and CD39$^+$CD103$^+$CD8$^+$ TILs for $n = 12$ patients; 95% confidence interval is shaded in gray (R, Spearman correlation; P value).

significantly more frequent in NR tumors than in CR tumors (**Fig. 5B** and **C**; Supplementary Fig. S10), which further corroborated the results of our histologic analysis.

Collectively, these results suggest that CR tumors have a preexisting immunoreactive contexture characterized by enrichment for tissue-resident, putatively tumor-reacting, early exhausted $CD8^+$ TILs. In contrast, an immunosuppressive contexture characterized by enrichment for Treg and M2-like tumor-associated macrophages (TAM) was identified in baseline NR tumors.

Differences in baseline circulating T and myeloid cell populations and soluble immune mediators distinguish CRs and NRs

In addition to analyzing the local immune TME, we also evaluated systemic immune markers associated with response to nCT in baseline PBMCs obtained from 16 patients with EAC in our prospective cohort. We used high-dimensional flow cytometry with 20 and 22 mAbs panels (panels N2 and N4, Supplementary Table S4) to assess T cell and myelomonocytic phenotypes, respectively (Supplementary Fig. S1). Unsupervised clustering analysis of T lymphocytes was performed separately for $CD4^+$ and $CD8^+$ T cells (Supplementary Figs. S11A and S11B and S12A and S12B), which revealed an increased frequency of exhausted $KLRG1^{high}$ $PD\text{-}1^{high}$ $CD4^+$ effector memory cells (#6; **Fig. 6A** and **B**; Supplementary Fig. S11B) and $TIGIT^{high}$ $PD\text{-}1^{high}$ $CD8^+$ transitional memory cells (#8; **Fig. 6C** and **D**; Supplementary Fig. S12B) in NR tumors. We also performed the unsupervised clustering analysis of 20 extracellular markers expressed by $CD45^+$ $CD3^-$ circulating immune cells and identified 11 distinct populations (**Fig. 6E**; Supplementary Fig. S13). In the pretreatment blood of NRs, there was a significant enrichment of monocytic myeloid-derived suppressor cells (MO-MDSC, cluster #4) expressing PD-L1 and CCR7 compared with CRs (**Fig. 6E–G**), suggesting that this population may suppress the antitumoral immune response and negatively affect the efficacy of nCT (36). Conversely, the pretreatment blood of CRs showed a higher frequency of putative inflammatory $CD14^+$ $CD11c^+$ $HLA\text{-}DR^{high}$ monocyte cluster (#1), indicating a potentially increased pool of immunostimulatory cells capable of infiltrating the tumor upon therapy (**Fig. 6E–G**). Notably, the frequency of this putative circulating inflammatory monocyte population was positively correlated with the frequency of putative tumor-reactive $CD39^+$ $CD103^+$ $CD8^+$ TILs, which characterizes baseline tumors in CRs (**Fig. 6H**).

Finally, we performed a comparison of the plasma concentration of 30 cytokines and chemokines in baseline blood samples from 26 patients of the prospective cohort (**Fig. 7**; Supplementary Figs. S1 and S14). Our analysis found that the plasma of CRs had higher concentrations of GM-CSF, a cytokine that positively affects the antitumor T lymphocyte response (**Fig. 7A**; ref. 37), whereas the plasma of NRs contained a significantly higher concentration of IL4, CXCL10, C3a, and C5a (**Fig. 7A**), the immune effectors associated with immunosuppression by MO-MDSCs (38–40). The frequency of putative antitumor $CD8^+$ $CD39^+$ $CD103^+$ TILs was positively correlated with the plasma concentration of GM-CSF, RANTES, and IL1RA, but was negatively correlated with IL4 concentration (**Fig. 7B** and **C**). In addition, the baseline frequency of the circulating putative inflammatory $CD14^+$ $CD11c^+$ $HLA\text{-}DR^{high}$ monocyte population was positively correlated with the baseline plasma concentration of GM-CSF (**Fig. 7D**). These results indicate that differential baseline immune determinants of response to nCT were also detectable in patients with EAC patients at the systemic level and were correlated with intratumor and systemic cellular immune parameters.

Discussion

In this study, we provide evidence that the preexisting immunity within baseline tumor tissues drives the clinical effects of nCT among patients with locally advanced EAC. These results strongly suggest that the immune composition of the TME prior to treatment impacts the outcomes of nCT.

Our study analyzed genomic data from baseline EAC biopsies and revealed that patients who showed a complete response to nCT had higher expression of immune response genes within their tumors. Our findings suggest that a functional MHC class I antigen presentation pathway is necessary to achieve a therapeutic response. Previous studies have linked a deficiency in the DNA damage and immune response (DDIR) pathway (41) and a higher nonsynonymous TMB (26) with a better response to nCT in EAC. Although we did not detect baseline DDIR signatures or higher TMB in our cohort of EAC responders to nCT, possibly due to the smaller sample size relative to previous studies (26, 41), the identified associations between immune-related pathways and response to nCT are mechanistically consistent with those studies.

Recent research has demonstrated an association between nCT response, baseline T-cell infiltration, and $CD8^+$ $PD\text{-}1^+$ staining scores in EAC (42, 43). Here, we utilized multiple approaches to gain a more comprehensive understanding of the immune landscape in baseline tumors, which was associated with a positive or negative therapeutic response to nCT at both local and systemic levels. Our findings revealed that CR tumors had a high frequency of tissue-resident memory $CD39^+$ $PD\text{-}1^+$ $CD8^+$ TILs, a population highly enriched for tumor antigen specificity and present in other solid tumors (33). Furthermore, we observed a high frequency of effector/memory $CD8^+$ TILs expressing T-bet and EOMES in CR tumors. This combination of transcription factors is characteristic of early exhausted TILs, which are capable of sustaining antitumor or chronic antiviral responses (34, 35). In contrast, our findings indicated that NR tumors had a predominantly suppressive immune contexture characterized by a high frequency of Treg cells and $CD163^+$ M2-like TAMs, both of which are associated with reduced patient OS. These results were consistent with recent reports (42), We also observed a higher frequency of circulating immunostimulatory $CD14^+$ $CD11c^+$ $HLA\text{-}DR^{high}$ monocytes in CRs, whereas NRs showed a higher frequency of circulating immunosuppressive $CCR7^+$ $PD\text{-}L1^+$ MO-MDSCs.

Using spatially resolved proteomic analysis of treatment-naïve EACs, we confirmed higher baseline levels of CD163 and FOXP3 in the tumor infiltrate of NR samples. In addition, the analysis revealed higher expression of the immune checkpoint inhibitor TIM3, which is expressed by Treg cells, enhancing the immunosuppressive function in cancer (44). Thus, in our study, increased levels of TIM3 were likely attributed to the higher frequency of Tregs seen in NRs, although the expression of TIM3 by other tumor-infiltrating immune populations cannot be completely ruled out. The DSP analysis also revealed significantly higher expression of STING in the immune-infiltrated stromal regions of NR tumors. Although STING induces anticancer IFN type I signaling, its activation in T cells may also prevent proliferation, promote cell death, and activate immune suppressive cells under certain conditions (45).

We also detected systemic differences in the blood samples of CRs versus NRs prior to treatment. Specifically, NRs had higher baseline plasma concentrations of suppressive cytokines CXCL10 and IL4, both of which may affect the migration and function of MDSCs (38, 39). Furthermore, NRs had significantly higher pre-nCT plasma concentrations of complement anaphylatoxins C3a and C5a, which

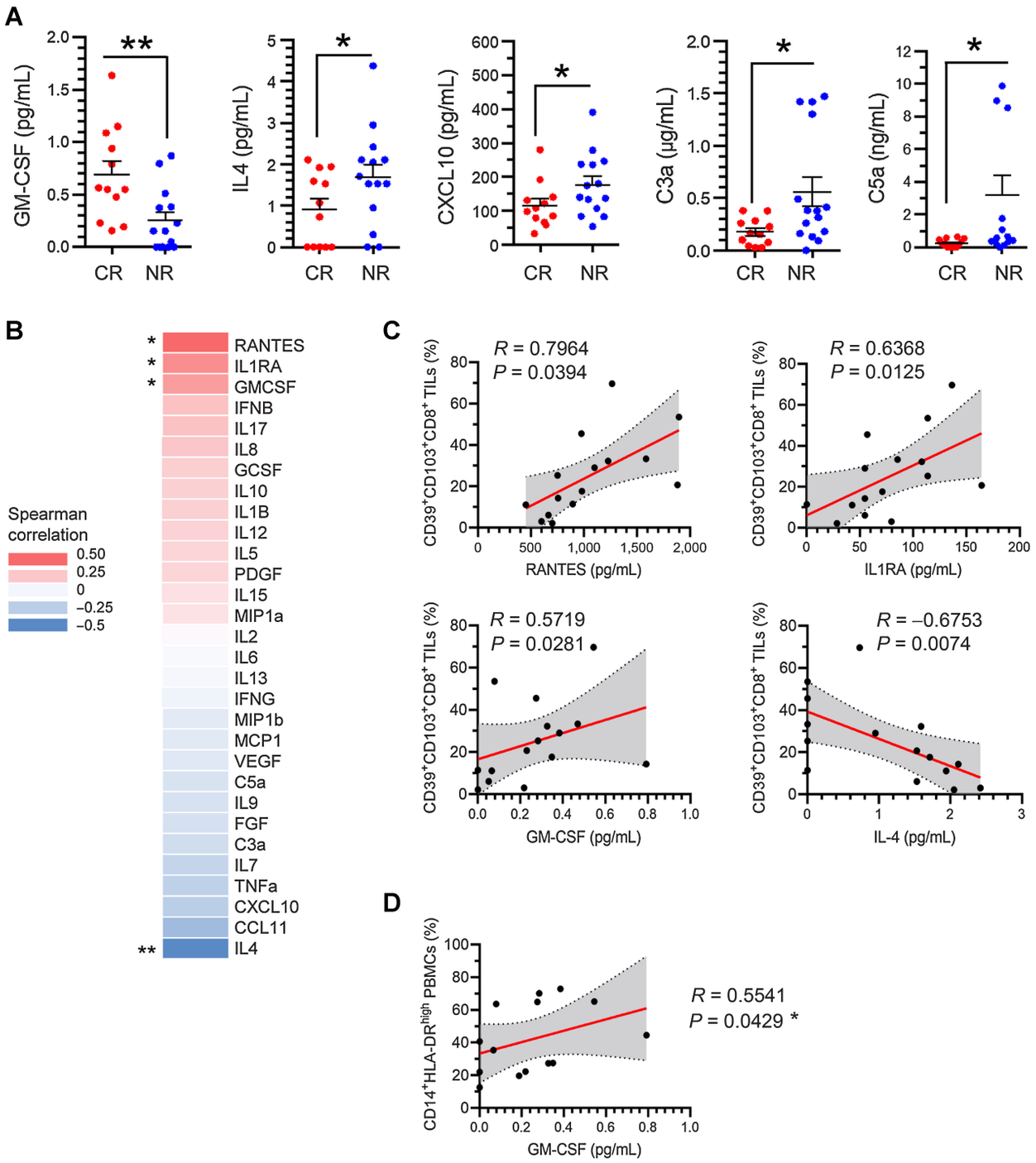

Figure 7.

Differential circulating proinflammatory cytokines and complement anaphylatoxins in responders and NRs to nCT. **A,** Baseline plasma concentrations of GM-CSF, IL4, CXCL10, C3a, and C5a in CRs ($n = 12$) and NRs($n = 14$); bars represent mean ± SEM. *, $P < 0.05$; **, $P < 0.01$; unpaired t test. **B,** Spearman correlation coefficients for the 30 circulating cytokines analyzed and frequency of tumor-infiltrating $CD8^+$ $CD39^+$ $CD103^+$ cells (calculated by flow cytometry manual gating on 15 baseline EACs; *, $P < 0.05$; **, $P < 0.01$). **C,** Correlation between the baseline plasma concentration of RANTES, IL1RA, GM-CSF, and IL4 and flow cytometry frequency (%) of $CD39^+$ $CD103^+$ $CD8^+$ TILs for $n = 15$ patients; 95% confidence interval (CI) is shaded in gray (R, Spearman correlation; P value). **D,** Correlation between the baseline plasma concentration of GM-CSF and flow cytometry frequency (%) of circulating $CD14^+$ $HLA\text{-}DR^{high}$ cells for $n = 15$ patients; 95% CI is shaded in gray (R, Spearman correlation; P value).

mediate the migration of suppressive immune cell populations within tumors and tumor-draining lymph nodes (40).

In addition to detecting distinct immune profiles, our multidimensional analysis revealed specific cancer cell-intrinsic differences between CRs and NRs. Specifically, baseline gene signatures were associated with cell cycle control in CRs, suggesting that the proliferative ability of cancer cells may impact treatment response to nCT. Similar pathways have also been shown to predict nCT responsiveness in $ER^+/HER2^-$ patient with breast cancer (46), although the underlying mechanisms are not fully understood. On the other hand, NR tumors were characterized by gene signatures correlated with lipid metabolism and peroxisomes, pathways associated with cancer resistance to chemo/radiation-induced damage and tumorigenesis (24, 47). The enrichment of a lipid metabolism genetic signature may be related not only to the metabolic requirements of the tumor but also to the functional profile of immune cells within the TME (48), which warrants further investigation. For instance, the activity of immune-suppressive cells such as Tregs and M2-like macrophages depends on fatty acid oxidation (49). Moreover, heightened lipid uptake and β-oxidation are characteristic of a hypoglycemic TME that is associated with poor tumor antigen presentation (50). Dysregulated cholesterol accumulation in the TME has also been linked to the induction of immunosuppressive cues (51), which is consistent with the suppressive immune contexture observed in EACs of NRs. These metabolic signatures represent potential vulnerabilities of cancer cells that could be targeted to reverse EAC resistance to nCT. In fact, several drugs are currently being investigated for targeting lipid metabolism in solid malignancies, such as gastric cancer (47), that could be combined with current nCT to improve their success rate.

Furthermore, our transcriptional analysis revealed significant enrichment of the long noncoding RNA SLC7A11-AS1 expression in CR tumors prior to nCT treatment. Previous studies have reported that SLC7A11-AS1 expression is correlated with the chemotherapy response in gastric cancer and, interestingly, with the suppression of *SLC7A11* gene expression (18). SLC7A11 is an antioxidant cystine/glutamate antiporter implicated in the inhibition of ferroptosis, an immunogenic cancer cell death induced by radiotherapy and the antitumor CD8 T-cell IFNγ response (19). Although further validation is needed, our findings hint at the fact that EAC cells may be resistant to nCT due to the inhibition of ferroptosis, which could potentially be targeted by certain drugs (19). Moreover, our DSP data revealed increased expression of the antiapoptotic protein Bcl2 and the stromal protein alpha SMA in cancer cells of NRs, suggesting increased baseline tumor resistance to apoptosis and its metastatic potential (29, 30). In addition, increased expression of alpha estrogen and progesterone receptors was observed in NR tumors, which could potentially be validated as markers of resistance to nCT and plausible therapeutic targets in future research.

The expression data obtained from NR tumors also revealed TIM3 as a potential candidate target for immune checkpoint blockade therapy. TIM3 is expressed by a variety of cell types, including Tregs, and its function is not solely attributed to immune suppression (44). Available clinical data have shown that blocking TIM3 in advanced treatment-refractory solid tumors, either alone or in combination with PD-1 or PD-L1 blockade, has only had modest antitumor activity (52). However, EAC was not included in these studies, and our data suggest that targeting TIM3 in this malignancy, either alone or in combination with PD-1 blockade and/or chemo/chemoradiotherapy (44), may represent a viable therapeutic option. Although our results are consistent with a model of nCT according to which it stimulates the preexisting spontaneous antitumor T-cell response, these treatments may also induce the antitumor T-cell response *de novo*. Indeed, clinical trials have demonstrated that some patients with EAC who did not respond to nCT showed positive response to adjuvant anti–PD-1 immunotherapy (53). Thus, exploring novel approaches for combining immunotherapies with chemotherapy, with or without radiotherapy, represents a promising avenue for further investigation (54). Validation of robust biomarkers will facilitate the identification of optimal patient candidates for receiving combination regimens. Notably, we observed a positive correlation between baseline infiltration of putative tumor-reactive $CD39^+$ $CD103^+$ $CD8^+$ TILs and circulating inflammatory HLA-DR^{high} monocytes in CRs. Furthermore, $CD39^+$ $CD103^+$ $CD8^+$ TILs showed a positive correlation with pretreatment circulating levels of the proinflammatory cytokines GM-CSF, IL1RA, and RANTES, and a negative correlation with IL4 concentration in the plasma. The detection of circulating MDSCs may also help distinguish CRs from NRs. Taken together, these systemic cellular and biochemical markers may represent a proxy for active tumor immune T-cell infiltration to serve as a predictor of response to nCT.

We acknowledge that the small number of patients included in our study is a limitation. However, the deep and comprehensive multidimensional analysis performed on paired tumor and blood samples from the same patients mitigates this limitation, as it possibly serves as one of the largest in-depth analyses of baseline EAC samples from a prospective cohort of patients. The results reported in this study are exploratory and hypothesis-generating, and rigorous validation in larger cohorts is needed. Moreover, the patients included in this study underwent two standard-of-care therapies for EAC, nCT alone or in combination with radiotherapy, both of which use platinum derivatives that have stimulatory effects on the antitumor immune response by either promoting immunogenic forms of cancer cell death or directly activating immune effector cells (7–9). Indeed, our baseline intratumor and systemic immune signatures, which predispose patients to respond to nCT, were consistent across both regimens, suggesting a shared mechanistic background between the two.

In conclusion, our study identifies novel potential immune markers and molecular pathways associated with therapeutic response or resistance to nCT in EAC. Further validation of these markers and pathways is needed to improve the prediction of response to nCT and guide the development of personalized therapeutic options.

Authors' Disclosures

No disclosures were reported.

Authors' Contributions

G. Arbore: Conceptualization, resources, data curation, formal analysis, supervision, funding acquisition, validation, investigation, visualization, methodology, writing–original draft, project administration, writing–review and editing. **L. Albarello:** Conceptualization, resources, data curation, formal analysis, validation, investigation, visualization, and methodology. **G. Bucci:** Conceptualization, resources, formal analysis, validation, investigation, and methodology. **M. Punta:** Conceptualization, resources, formal analysis, validation, investigation, and methodology. **A. Cossu:** Resources, data curation, supervision, and investigation. **L. Fanti:** Resources and investigation. **A. Maurizio:** Resources, formal analysis, validation, investigation, and methodology. **F. Di Mauro:** Data curation and investigation. **V. Bilello:** Formal analysis and methodology. **G. Arrigoni:** Formal analysis, investigation, and methodology. **S. Bonfiglio:** Conceptualization, resources, data curation, and methodology. **D. Biancolini:** Resources and methodology. **F. Puccetti:** Resources and methodology. **U. Elmore:** Resources and investigation. **L. Vago:** Resources andmethodology. **S. Cascinu:** Conceptualization and methodology. **G. Tonon:** Conceptualization, resources, investigation, and methodology. **R. Rosati:** Conceptualization, resources, supervision, funding acquisition, and investigation. **G. Casorati:** Conceptualization, resources, supervision, funding acquisition,

investigation, methodology, and writing-original draft. **P. Dellabona:** Conceptualization, resources, supervision, funding acquisition, investigation, methodology, writing–original draft, and project administration.

Acknowledgments

This study was supported by the European Molecular Biology Organization grant ALTF 1358–2016, European Commission Marie Curie Individual Fellowship Grant IC_IL_EC_2017, L'Oréal UNESCO for Women in Science Italy, and Italian Association for Cancer Research Grant MFAG 24780. The authors thank the staff of the Gastrointestinal Surgery Unit at San Raffaele Hospital for their support in patient enrollment and clinical sample collection, the staff of the Center for OMICs Sciences at San Raffaele Institute for their feedback on the sample processing and the analysis of next-generation sequencing data, Drs. Claudia De Lalla and Cristina Faccani from the Experimental Immunology Unit at San Raffaele Institute for their feedback on the analysis of high-dimensional flow cytometry data, and the patients participating to the ESOCA-001, DSAN 718/1F, and DSAN 0565/5TF studies.

The publication costs of this article were defrayed in part by the payment of publication fees. Therefore, and solely to indicate this fact, this article is hereby marked "advertisement" in accordance with 18 USC section 1734.

Note

Supplementary data for this article are available at Cancer Research Online (http://cancerres.aacrjournals.org/).

Received February 2, 2023; revised May 18, 2023; accepted June 20, 2023; published first June 23, 2023.

References

1. Smyth EC, Lagergren J, Fitzgerald RC, Lordick F, Shah MA, Lagergren P, et al. Oesophageal cancer. Nat Rev Dis Primers 2017;3:17048.
2. Shapiro J, van Lanschot JJB, Hulshof M, van Hagen P, van Berge Henegouwen MI, Wijnhoven BPL, et al. Steyerberg EW, van der Gaast A; CROSS study group. Neoadjuvant chemoradiotherapy plus surgery versus surgery alone for oesophageal or junctional cancer (CROSS): long-term results of a randomised controlled trial. Lancet Oncol 2015;16:1090–8.
3. Obermannová R, Alsina M, Cervantes A, Leong T, Lordick F, Nilsson M, et al. Oesophageal cancer: ESMO Clinical Practice Guideline for diagnosis, treatment and follow-up. Ann Oncol 2022;33:992–1004.
4. Fridman WH, Pagès F, Sautès-Fridman C, Galon J. The immune contexture in human tumours: impact on clinical outcome. Nat Rev Cancer 2012;12:298–306.
5. Mennonna D, Maccalli C, Romano MC, Garavaglia C, Capocefalo F, Bordoni R, et al. T cell neoepitope discovery in colorectal cancer by high throughput profiling of somatic mutations in expressed genes. Gut 2017;66:454–63.
6. Ribas A, Wolchok JD. Cancer immunotherapy using checkpoint blockade. Science 2018;359:1350–5.
7. Galluzzi L, Senovilla L, Zitvogel L, Kroemer G. The secret ally: immunostimulation by anticancer drugs. Nat Rev Drug Discov 2012;11:215–33.
8. Lhuillier C, Rudqvist NP, Elemento O, Formenti SC, Demaria S. Radiation therapy and anti-tumor immunity: exposing immunogenic mutations to the immune system. Genome Med 2019;11:40.
9. Kroemer G, Galassi C, Zitvogel L, Galluzzi L. Immunogenic cell stress and death. Nat Immunol 2022;23:487–500.
10. Mandard AM, Dalibard F, Mandard JC, Marnay J, Henry-Amar M, Petiot JF, et al. Pathologic assessment of tumor regression after preoperative chemoradiotherapy of esophageal carcinoma. Clinicopathologic correlations. Cancer 1994;73:2680–6.
11. Donahue JM, Nichols FC, Li Z, Schomas DA, Allen MS, Cassivi SD, et al. Complete pathologic response after neoadjuvant chemoradiotherapy for esophageal cancer is associated with enhanced survival. Ann Thorac Surg 2009;87:392–8; discussion 398–9.
12. Chen Y, Hao Q, Wang J, Li J, Huang C, Zhang Y, et al. Ubiquitin ligase TRIM71 suppresses ovarian tumorigenesis by degrading mutant p53. Cell Death Dis 2019;10:737.
13. Jordan MS, Koretzky GA. Coordination of receptor signaling in multiple hematopoietic cell lineages by the adaptor protein SLP-76. Cold Spring Harb Perspect Biol 2010;2:a002501.
14. Wang Z, Peng M. A novel prognostic biomarker LCP2 correlates with metastatic melanoma-infiltrating CD8+ T cells. Sci Rep 2021;11:9164.
15. Dollt C, Michel J, Kloss L, Melchers S, Schledzewski K, Becker K, et al. The novel immunoglobulin super family receptor SLAMF9 identified in TAM of murine and human melanoma influences pro-inflammatory cytokine secretion and migration. Cell Death Dis 2018;9:939.
16. Wang L, Yin J, Wang X, Shao M, Duan F, Wu W, et al. C-type lectin-like receptor 2 suppresses AKT signaling and invasive activities of gastric cancer cells by blocking expression of phosphoinositide 3-kinase subunits. Gastroenterology 2016;150:1183–95.
17. Hu R, Bi R, Jiang L, Yang X, Zhong Y, Xie X. LncRNA TUSC8 suppresses the proliferation and migration of esophageal cancer cells by downregulation of VEGFA. J Cancer 2021;12:6393–400.
18. Luo Y, Xiang W, Liu Z, Yao L, Tang L, Tan W, et al. Functional role of the SLC7A11-AS1/xCT axis in the development of gastric cancer cisplatin-resistance by a GSH-dependent mechanism. Free Radic Biol Med 2022;184:53–65.
19. Lang X, Green MD, Wang W, Yu J, Choi JE, Jiang L, et al. Radiotherapy and immunotherapy promote tumoral lipid oxidation and ferroptosis via synergistic repression of SLC7A11. Cancer Discov 2019;9:1673–85.
20. Han W, Hu C, Fan ZJ, Shen GL. Transcript levels of keratin 1/5/6/14/15/16/17 as potential prognostic indicators in melanoma patients. Sci Rep. 2021;11:1023.
21. Iwabu J, Yamashita S, Takeshima H, Kishino T, Takahashi T, Oda I, et al. FGF5 methylation is a sensitivity marker of esophageal squamous cell carcinoma to definitive chemoradiotherapy. Sci Rep 2019;9:13347.
22. Toivola DM, Boor P, Alam C, Strnad P. Keratins in health and disease. Curr Opin Cell Biol 2015;32:73–81.
23. Lee YE, He HL, Shiue YL, Lee SW, Lin LC, Wu TF, et al. The prognostic impact of lipid biosynthesis-associated markers, HSD17B2 and HMGCS2, in rectal cancer treated with neoadjuvant concurrent chemoradiotherapy. Tumour Biol 2015;36:7675–83.
24. Luis G, Godfroid A, Nishiumi S, Cimino J, Blacher S, Maquoi E, et al. Tumor resistance to ferroptosis driven by Stearoyl-CoA Desaturase-1 (SCD1) in cancer cells and Fatty Acid Biding Protein-4 (FABP4) in tumor microenvironment promote tumor recurrence. Redox Biol 2021;43:102006.
25. Dahabieh MS, Di PE, Jangal M, Goncalves C, Witcher M, Braverman NE, et al. Peroxisomes and cancer: The role of a metabolic specialist in a disease of aberrant metabolism. Biochim Biophys Acta Rev Cancer 2018;1870:103–21.
26. Izadi F, Sharpe BP, Breininger SP, Secrier M, Gibson J, Walker RC, et al. Genomic analysis of response to neoadjuvant chemotherapy in esophageal adenocarcinoma. Cancers (Basel) 2021;13:3394.
27. Dhatchinamoorthy K, Colbert JD, and Kenneth L. Rock KL. Cancer immune evasion through loss of MHC class I antigen presentation. Front Immunol 2021;12:636568.
28. McGranahan N, Rosenthal R, Hiley CT, Rowan AJ, Watkins TBK, Wilson GA, et al. Allele-specific HLA loss and immune escape in lung cancer evolution. Cell 2017;171:1259–71.
29. Cory S, Huang DC, Adams JM. The Bcl-2 family: roles in cell survival and oncogenesis. Oncogene 2003;22:8590–607.
30. Pearce OMT, Delaine-Smith RM, Maniati E, Nichols S, Wang J, Böhm S, et al. Deconstruction of a metastatic tumor microenvironment reveals a common matrix response in human cancers. Cancer Discov 2018;8:304–19.
31. Al-Khyatt W, Tufarelli C, Khan R, Iftikhar SY. Selective oestrogen receptor antagonists inhibit oesophageal cancer cell proliferation in vitro. BMC Cancer 2018;18:121.
32. Li M, Zhou C. Progesterone receptor gene serves as a prognostic biomarker associated with immune infiltration in gastric cancer: a bioinformatics analysis. Transl Cancer Res 2021;10:2663–77.
33. Duhen T, Duhen R, Montler R, Moses J, Moudgil T, de Miranda NF, et al. Co-expression of CD39 and CD103 identifies tumor-reactive CD8 T cells in human solid tumors. Nat Commun 2018;9:2724.
34. Losurdo A, Scirgolea C, Alvisi G, Brummelman J, Errico V, Di Tommaso L, et al. Single-cell profiling defines the prognostic benefit of CD39high tissue

resident memory CD8+ T cells in luminal-like breast cancer. Commun Biol 2021;4:1117.
35. McLane LM, Abdel-Hakeem MS, Wherry EJ. CD8 T cell exhaustion during chronic viral infection and cancer. Annu Rev Immunol 2019;37:457–95.
36. Shields JD, Kourtis IC, Tomei AA, Roberts JM, Swartz MA. Induction of lymphoidlike stroma and immune escape by tumors that express the chemokine CCL21. Science 2010;328:749–52.
37. Zarei S, Schwenter F, Luy P, Aurrand-Lions M, Morel P, Kopf M, et al. Role of GM-CSF signaling in cell-based tumor immunization. Blood 2009;113:6658–68.
38. Mandruzzato S, Solito S, Falisi E, Francescato S, Chiarion-Sileni V, Mocellin S, et al. IL4Ralpha+ myeloid-derived suppressor cell expansion in cancer patients. J Immunol 2009;182:6562–8.
39. Liu H, Ling CC, Yeung WHO, Pang L, Liu J, Zhou J, et al. Monocytic MDSC mobilization promotes tumor recurrence after liver transplantation via CXCL10/TLR4/MMP14 signaling. Cell Death Dis 2021;12:489.
40. Llaudo I, Fribourg M, Medof ME, Conde P, Ochando J, Heeger PS. C5aR1 regulates migration of suppressive myeloid cells required for costimulatory blockade-induced murine allograft survival. Am J Transplant 2019;19:633–45.
41. Turkington RC, Knight LA, Blayney JK, Secrier M, Douglas R, Parkes EE, et al. Immune activation by DNA damage predicts response to chemotherapy and survival in oesophageal adenocarcinoma. Gut 2019;68:1918–27.
42. Goedegebuure RSA, Harrasser M, de Klerk LK, van Schooten TS, van Grieken NCT, Eken M, et al. Pre-treatment tumor-infiltrating T cells influence response to neoadjuvant chemoradiotherapy in esophageal adenocarcinoma. Oncoimmunology 2021;10:1954807.
43. Soeratram TT, Creemers A, Meijer SL, de Boer OJ, Vos W, Hooijer GK, et al. Tumor-immune landscape patterns before and after chemoradiation in resectable esophageal adenocarcinomas. J Pathol 2022;256:282–96.
44. Tian T, Li Z. Targeting Tim-3 in cancer with resistance to PD-1/PD-L1 blockade. Front Oncol 2021;11:731175.
45. Cerboni S, Jeremiah N, Gentili M, Gehrmann U, Conrad C, Stolzenberg MC, et al. Intrinsic antiproliferative activity of the innate sensor STING in T lymphocytes. J Exp Med 2017;214:1769–85.
46. Oshi M, Takahashi H, Tokumaru Y, Yan L, Rashid OM, Nagahashi M, et al. The E2F pathway score as a predictive biomarker of response to neoadjuvant therapy in ER+/HER2- breast cancer. Cells 2020;9:1643.
47. Bacci M, Lorito N, Smiriglia A, Morandi A. Fat and furious: lipid metabolism in antitumoral therapy response and resistance. Trends Cancer 2021;7:198–213.
48. Leone RD, Powell JD. Metabolism of immune cells in cancer. Nat Rev Cancer 2020;20:516–31.
49. Arner EN, Rathmell JC. Metabolic programming and immune suppression in the tumor microenvironment. Cancer Cell 2023;41:421–33.
50. Pedrosa L, Foguet C, Oliveres H, Archilla I, de Herreros MG, Rodríguez A, et al. A novel gene signature unveils three distinct immune-metabolic rewiring patterns conserved across diverse tumor types and associated with outcomes. Front Immunol 2022;13:926304.
51. Ma X, Bi E, Lu Y, Su P, Huang C, Liu L, et al. Cholesterol induces CD8+ T cell exhaustion in the tumor microenvironment. Cell Metab 2019;30:143–56.
52. Harding JJ, Moreno V, Bang YJ, Hong MH, Patnaik A, Trigo J, et al. Blocking TIM-3 in treatment-refractory advanced solid tumors: a phase Ia/b study of LY3321367 with or without an Anti-PD-L1 antibody. Clin Cancer Res 2021;27:2168–78.
53. Kelly RJ, Ajani JA, Kuzdzal J, Zander T, Van Cutsem E, Piessen G, et al. Adjuvant nivolumab in resected esophageal or gastroesophageal junction cancer. N Engl J Med 2021;384:1191–203.
54. van den Ende T, de Clercq NC, van Berge Henegouwen MI, Gisbertz SS, Geijsen ED, Verhoeven RHA, et al. Neoadjuvant chemoradiotherapy combined with atezolizumab for resectable esophageal adenocarcinoma: a single-arm phase II feasibility trial (PERFECT). Clin Cancer Res 2021;27:3351–9.